Nanoparticle Superlattices as Efficient Bifunctional Electrocatalysts for Water Splitting

Jun Li,[†,⊥] Yongcheng Wang,[†,⊥] Tong Zhou,[‡] Hui Zhang,[§] Xuhui Sun,[§] Jing Tang,[†] Lijuan Zhang,[†] Abdullah M. Al-Enizi,[∥] Zhongqin Yang,[‡] and Gengfeng Zheng*,[†]

[†]Laboratory of Advanced Materials, Department of Chemistry, Collaborative Innovation Center of Chemistry for Energy Materials and [‡]State Key Laboratory of Surface Physics, Key Laboratory for Computational Physical Sciences (MOE) and Department of Physics, Fudan University, Shanghai 200433, China

[§]Soochow University-Western University Centre for Synchrotron Radiation Research, Institute of Functional Nano and Soft Materials Laboratory, Collaborative Innovation Center of Suzhou Nano Science and Technology, Soochow University, Suzhou, Jiangsu 215123, China

[∥]Department of Chemistry, College of Science, King Saud University, Riyadh 11451, Saudi Arabia

S *Supporting Information*

ABSTRACT: The solar-driven water splitting process is highly attractive for alternative energy utilization, while developing efficient, earth-abundant, bifunctional catalysts for both oxygen evolution reaction and hydrogen evolution reaction has remained as a major challenge. Herein, we develop an ordered CoMnO@CN superlattice structure as an efficient bifunctional water-splitting electrocatalyst, in which uniform Co−Mn oxide (CoMnO) nanoparticles are coated with a thin, continuous nitrogen-doped carbon (CN) framework. The CoMnO nanoparticles enable optimized OER activity with effective electronic structure configuration, and the CN framework serves as an excellent HER catalyst. Importantly, the ordered superlattice structure is beneficial for enhanced reactive sites, efficient charge transfer, and structural stability. This bifunctional superlattice catalyst manifests optimized current densities and electrochemical stability in overall water splitting, outperforming most of the previously reported single- or bifunctional electrocatalysts. Combining with a silicon photovoltaic cell, this CoMnO@CN superlattice bifunctional catalyst enables unassisted solar water splitting continuously for ∼5 days with a solar-to-hydrogen conversion efficiency of ∼8.0%. Our discovery suggests that these transition metal oxide-based superlattices may serve as a unique structure modality for efficient bifunctional water splitting electrocatalysts with scale-up potentials.
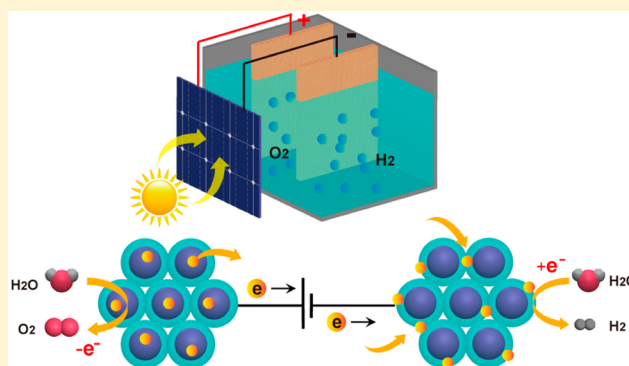
■ INTRODUCTION

Hydrogen fuel generated by electrochemical water splitting represents one of the most attractive chemical methods for renewable energy storage.[1−8] When further coupled with solar energy capture and conversion, this electrocatalytic water splitting approach may enable direct utilization of unlimited solar energy with minimum carbon footprint in the environment.[3,4] Central to the ongoing research efforts is the realization of efficient electrocatalysts that can effectively enhance sluggish kinetic processes and allow for both water reduction and oxidation at low overpotentials. Pt[9] and noble metal oxides (e.g., IrO_2, RuO_2)[10] are regarded as pioneering hydrogen evolution reaction (HER) and oxygen evolution reaction (OER) catalysts, respectively, and can be processed in a large window of solution pHs with high efficiencies, while the capability of large-scale application is prohibited by the lack of supply and high cost of these materials. Alternatively, the first-row transition metal oxides and sulfides are currently intensively investigated to improve the intrinsic activity as potential earth-abundant material candidates for water splitting electrocatalysts.[5,6] Moreover, single bifunctional material composites capable of catalyzing both OER and HER are extremely attractive and have been demonstrated recently, such as NiFe layered double hydroxides (LDHs),[7] cobalt/cobalt oxide/N-doped carbon hybrids,[11] $NiFeO_x$ nanoparticles,[12] Co−P derived film,[13,14] and NiSe nanowire film,[15] which reduce the need and cost associated with separate equipment and processes for different catalysts.[7] Due to their generally insulating nature, tendency to aggregate, and poor chemical stability,[16] these LDHs and nanoparticles are usually enhanced by incorporating conducting reagents, such as carbon nanotubes[17,18] and graphene,[19] to improve the charge transport and stability. Nonetheless, with the increase of catalyst surface
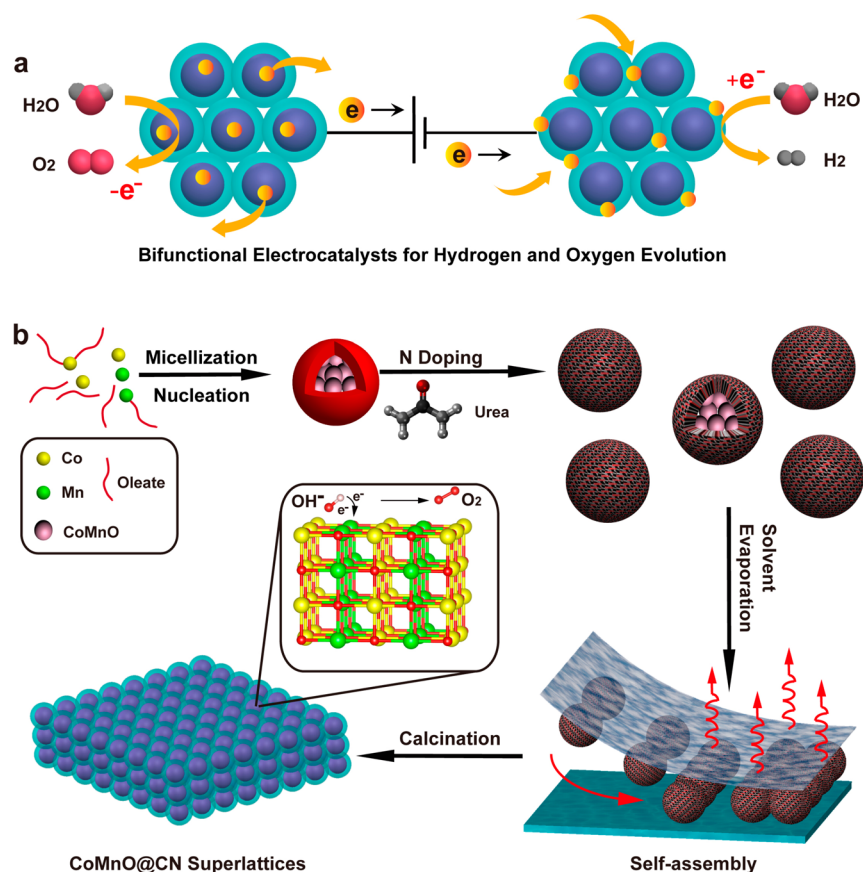
Figure 1. Schemes. (a) Design of the CoMnO@CN superlattices as a bifunctional OER and HER catalyst. The ordered CoMnO nanoparticles serve as the OER catalytic sites for water oxidation, and the nitrogen-doped carbon framework serves as the HER catalytic sites for water reduction. (b) Synthesis procedures of the CoMnO@CN superlattices, including micellization, nucleation, nitrogen (N) doping, solvent evaporation, and calcination.

loading, the lack of long-range structure/order control of these material composites inevitably limits the increase of surface reactive sites and charge transport capability, thus posing a substantial barrier on the realization of effective bifunctional electrocatalysts with scalability.

Three-dimensional (3D) superlattices composed of ordered, close-packed nanoparticles feature high surface area, abundant active sites, and collective properties that differ from isolated/disordered nanoparticles.[20] The bottom-up solution approach enables the synthesis of multivalent nanoparticle assembly with versatile composition/structures, high uniformity, and long-range order.[21] Furthermore, it has recently been demonstrated that the poor intrinsic electrical conductivity of individual nanoparticles can be improved by direct incorporation of conducting carbon frameworks between neighboring nanoparticles during superlattice synthesis.[22] These features thus greatly inspire the rational design of 3D nanoparticle/carbon superlattices as bifunctional water-splitting electrocatalysts. The interplay between carbon and metal oxide nanoparticles can modify the overall physicochemical and electronic structures to favor the electron transfer at the interface, with capabilities of enhanced coupling between close-packed nanoparticles and tunable doping for optimized performances.

In this paper, we develop a highly ordered carbon-coated Co−Mn oxide nanoparticle superlattice by a solvent evaporation-induced self-assembly method followed by annealing, during which nitrogen dopants are further incorporated into the carbon framework in the superlattices (designated as CoMnO@CN). The obtained CoMnO@CN superlattices are endowed with several attractive features (Figure 1a). For the morphology design, the interconnected nanoparticle superlattice structure can increase the number of reactive sites while retaining high conductivity and structure stability. On the electronic structure, the constituents of CoMnO@CN have a collective effect to enhance electrocatalyst performances. The CoMnO nanoparticles with octahedral Co^{2+} and tunable Mn doping levels offer an optimized electronic structure for OER. The presence of metal oxide nanoparticles inside carbon framework contributes to the decrease of local work function on the carbon surface, due to facile electron transfer beneficial for HER.[23,24] The nitrogen-doped carbon (CN) framework has an excellent electronic structure for HER,[25,26] while at the same time serving as a uniform layer to enhance charge transport of CoMnO nanoparticles and prevent them from aggregation. Thus, this CoMnO@CN superlattice structure efficiently enables both OER and HER catalysis in the same alkaline electrolyte, with optimized overpotentials of 263 and 71 mV at 20 mA·cm^{-2} for OER and HER, respectively, comparable to the best reported earth-abundant material-based OER and HER catalysts.[3,17] More importantly, due to the long-range order of the superlattice networks that facilitate the charge transfer and reactive surface exposure, this CoMnO@CN superlattice structure maintains a high electrocatalytic activity at much higher catalyst loading, which exceeds most of the previously reported individual OER or HER catalysts, suggesting the potential of utilizing this bifunctional electrocatalyst for solar
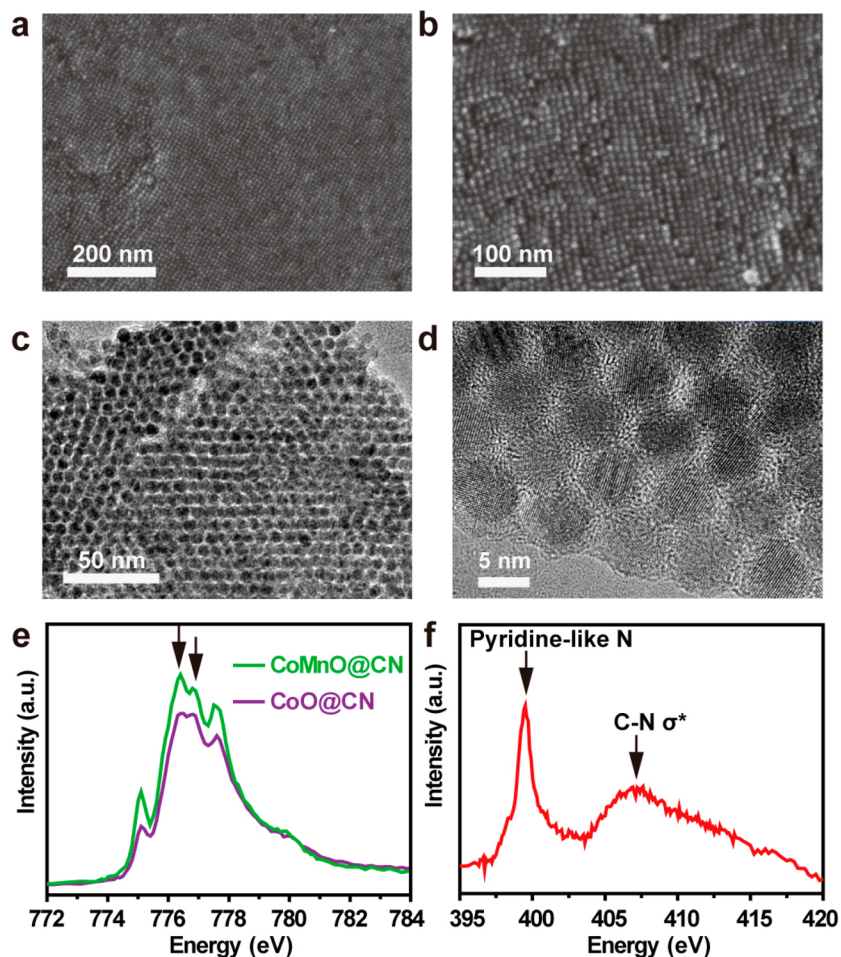
Figure 2. Structural characterizations. (a, b) SEM and (c, d) TEM images of the CoMnO@CN superlattices. (e) The Co L_3-edge NEXAFS of the CoO@CN and CoMnO@CN superlattices. (f) Nitrogen K-edge NEXAFS of the CoMnO@CN superlattices.

energy-driven water splitting. As a proof-of-concept, when coupled with a commercial solar cell with a photoconversion efficiency of ~16%, a two-electrode electrolyzer coated with this bifunctional superlattice electrocatalyst exhibits a stable current density of 6.4 mA·cm^{-2} for ~5 days, with a solar-to-hydrogen conversion efficiency of ~8.0%.

■ RESULTS AND DISCUSSION

Synthesis and Structural Characterization. The CoMnO@CN superlattices were synthesized by a solvent evaporation-induced self-assembly method (Methods in the Supporting Information, Figure 1b). Monodisperse CoMnO nanoparticles with surface-coated oleic acid ligands were first synthesized from a cobalt/manganese—oleate complex precursor via a micellization and nucleation process,[27−29] which is critical for the subsequent assembly of highly ordered superlattices. Then urea was further added to the as-prepared monodispersed CoMnO nanoparticles for the subsequent nitrogen doping. With a slow evaporation of solvent, the oleic acid-coated CoMnO nanoparticles were assembled into a highly ordered superlattice structure, which was subsequently calcinized to convert the surface oleic acid and urea ligands into a nitrogen-doped carbon (CN) framework. The ratio of the two metal ions was facilely tuned by varying the precursors employed, and the Co/Mn ratio in the final nanoparticle superlattices was determined by ion-conductive plasma (ICP).

For equal moles of Co and Mn in the precursors, the resultant CoMnO@CN superlattices have a Co/Mn ratio of 1.4:1. The formation of stable CoMnO@CN superlattices can be attributed to the effective separation of nucleation and self-assembly processes, which subsequently contribute to long-range structural ordering of the interconnected superlattices, strongly coupled interaction between constituent ions, and the 3D crystal-like morphology.[30]

Scanning electron microscopy (SEM) images show that the CoMnO@CN superlattices retain a closely packed nanoparticle assembly with long-range ordering (Figure 2a, b). Few cracks, agglomeration, or other defects are observed over a large range of the superlattice structure, suggesting a high thermal stability of the interconnected CoMnO@CN superlattices.[31,32] Transmission electron microscopy (TEM) images manifest the ordered assembly of nanoparticles (Figure 2c, d), which present a face-centered-cubic (fcc) structure.[22] The nanoparticles have a uniform diameter of ~5 nm, embedded and separated by an amorphous carbon layer of ~2 nm. The X-ray diffraction (XRD, Figure S1) pattern of the CoMnO@CN superlattice powder shows diffraction peaks that are indexed to the complex oxides of CoO (PDF# 01-074-2392) and MnO (PDF# 00-001-1206) and a small amount of MnCo$_2$O$_4$ (PDF# 00-023-1237).

To further verify the electronic structure of the catalyst, the samples were characterized by Near Edge X-ray Absorption Fine Structure (NEXAFS) spectroscopy. The Co L_3-edge
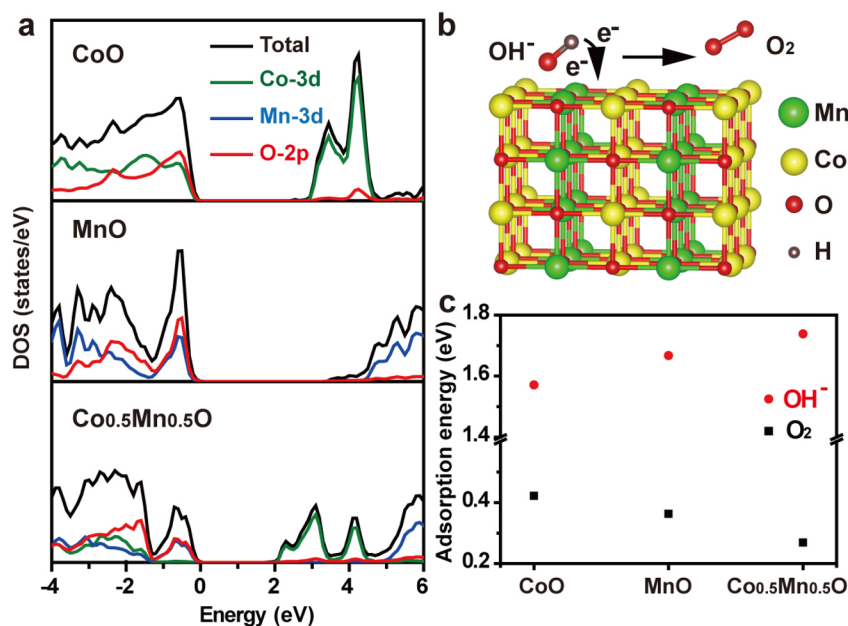
Figure 3. Calculations of structures and reactivity. (a) The total DOS and the PDOS of CoO, MnO, and $Co_{0.5}Mn_{0.5}O$. (b) Schematic model of OH^- adsorption and oxygen release on $Co_{0.5}Mn_{0.5}O$ (001) surface. (c) Calculated adsorption energies of OH^- (red dots) and O_2 (black dots) on CoO, MnO, and $Co_{0.5}Mn_{0.5}O$ (001) surfaces.

spectrum of the CoO sample (Figure 2e) is ascribed to the Co^{2+} with an octahedral (O_h) structure.[16,34] The addition of Mn content increases the intensity of L_3 features, and the peaks at 776.4 and 776.8 eV of the Co L_3-edge (arrows in Figure 2e) become more prominent, indicating that the Mn^{2+} incorporation elevates the content of the unoccupied Co 3d state as well as distorts the Co^{2+} coordination, thus allowing for enhanced OER capability.[16,34,35] The peak at 631.9 eV in the Mn $L_{3,2}$-edge NEXAFS shows most of the Mn species in both the MnO@CN and CoMnO@CN superlattices are Mn^{2+} (Figure S2).[36] Moreover, the K-edge NEXAFS of nitrogen in the CoMnO@CN sample was analyzed to investigate the nitrogen doping effect (Figure 2f). The peaks at 398.6 and 406.8 eV are ascribed to pyridine-like N and C−N, respectively, and the pyridine-like N is the dominant N due to the high peak intensity. Energy dispersive X-ray (EDX) spectroscopy shows the content of N is 1.76%, consistent with previous reports using similar N doping strategies.[11]

In addition, CoO@CN and MnO@CN superlattices, as well as different Co/Mn ratios, were obtained with similar ordered structures. In contrast, CoMnO@CN nanoparticles synthesized without the initial micellization and nucleation procedures do not present an ordered structure (designated as disordered CoMnO@CN nanoparticles, Figure S3). This lack of long-range ordering is ascribed to the simultaneous nucleation and assembly of nanoparticles during thermolysis, in which nanoparticles tend to sinter and agglomerate at elevated temperatures.[20,33] The effective active surface areas of the ordered and disordered CoMnO@CN catalysts were evaluated by measuring their cyclic voltammograms (CVs, Figure S4) and the electrochemically active surface areas (Methods in the Supporting Information).[11,37] The CoMnO@CN superlattices present a large double-layer capacitance (114 mF·cm^{-2}), which is >5 times higher than the disordered CoMnO@CN nanoparticles (21 mF·cm^{-2}), suggesting that the highly ordered superlattice structure is beneficial for exposure of surface reactive sites.

Calculation of Structures and Reactivity. The Mn doping effect on the electronic structure of CoO was first illustrated by density-functional theory (DFT) calculations, in which 2 × 2 × 2 supercells with 8 × 8 × 8 mesh of k-points were used to calculate the O_h structures of CoO, MnO, and $Co_{0.5}Mn_{0.5}O$ (where, as a model example, 50% of Co positions are replaced by Mn, Figure S5). The total densities of states (DOSs) and the projected densities of states (PDOSs) of CoO, MnO, and $Co_{0.5}Mn_{0.5}O$ are plotted (Figure 3a). For CoO and MnO, the valence band edges are mostly composed of O 2p states, and the conduction band edges mainly consist of corresponding metal 3d states, consistent with previous studies.[38] The calculated bandgaps for CoO and MnO are 2.8 and 3.4 eV, respectively, in good agreement with experimental values.[38,39] For $Co_{0.5}Mn_{0.5}O$, the conduction band edge shifts toward the negative direction by ~0.8 eV, resulting in a bandgap of 2.0 eV. This bandgap narrowing leads to the enhanced excitation of charge carriers to the conduction band,[40] which is beneficial for the electrical conductivity increase and the electrochemical performances of the catalyst.

The adsorption properties of OH^- and O_2 on these metal oxide surfaces were further calculated to evaluate the effect of the electronic structures on OER. The optimized structures show that the O atom of OH^- and O_2 are bonded with metal atoms of metal oxide (001) surfaces (Figure 3b). The bond length between OH^- and $Co_{0.5}Mn_{0.5}O$ is 1.84 Å (Figure S6, red dots), shorter than that of pristine CoO and MnO, suggesting $Co_{0.5}Mn_{0.5}O$ has a stronger capability of adsorbing OH^-. Correspondingly, the calculated adsorption energies of OH^- (E_{OH^-}) of $Co_{0.5}Mn_{0.5}O$ is 1.74 eV, larger than that of pristine CoO and MnO (Figure 3c, red dots), confirming the enhanced probability and stability of adsorbed OH^- on $Co_{0.5}Mn_{0.5}O$. In addition, the bond length between O_2 and $Co_{0.5}Mn_{0.5}O$ is calculated as 2.31 Å (Figure S6, black dots), larger than that of CoO and MnO, and the corresponding adsorption energy of O_2 (E_{O_2}) on $Co_{0.5}Mn_{0.5}O_2$ is lower than that of CoO and MnO (Figure 3c, black dots). This longer bond length and lower
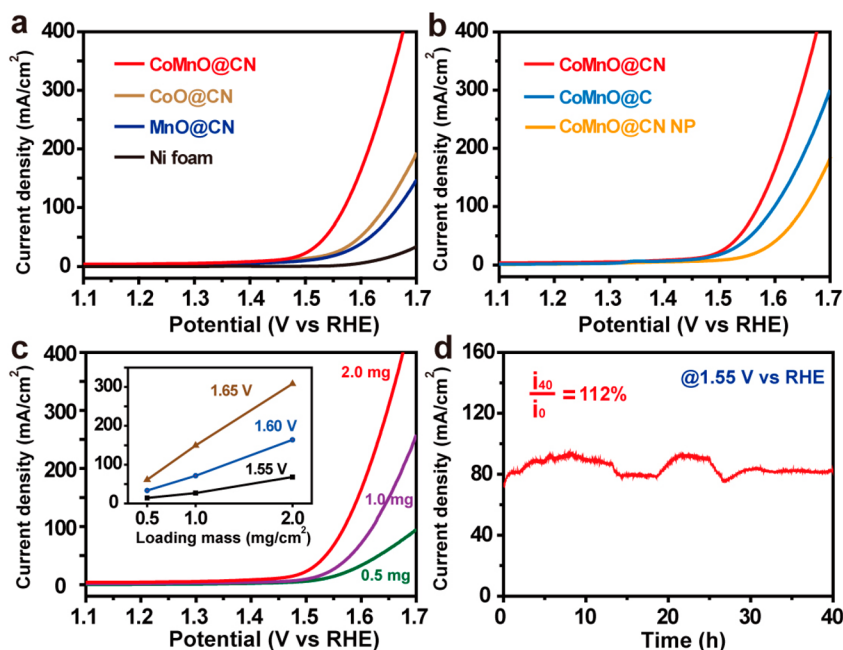
Figure 4. OER electrocatalytic performances. (a) LSV curves for OER of the CoMnO@CN (red curve), CoO@CN (brown curve), and MnO@CN (blue curve) superlattices. The LSV of a blank Ni foam electrode is also plotted as a control (black curve). (b) LSV curves for OER of the CoMnO@CN (red curve), CoMnO@C (blue curve) superlattices, and disordered CoMnO@CN nanoparticles (orange curve). The loading of each catalyst in (a, b) was ~2.0 mg·cm^{-2}. (c) The OER activities of the CoMnO@CN superlattices at different loadings of 0.5, 1.0, and 2.0 mg·cm^{-2}. Inset: specific current densities at 1.55, 1.60, and 1.65 V vs RHE of the CoMnO@CN superlattices at different loading masses of 0.5, 1.0, and 2.0 mg·cm^{-2}, respectively. (d) Chronoamperometric measurement of the CoMnO@CN superlattice catalyst at 1.55 V vs RHE.

adsorption energy between O_2 and metal ions increase the probability of releasing O_2 from metal oxide surface. Combining with the aforementioned band structures, these calculation results suggest that Co−Mn oxide has an optimal electronic structure as an OER catalyst.
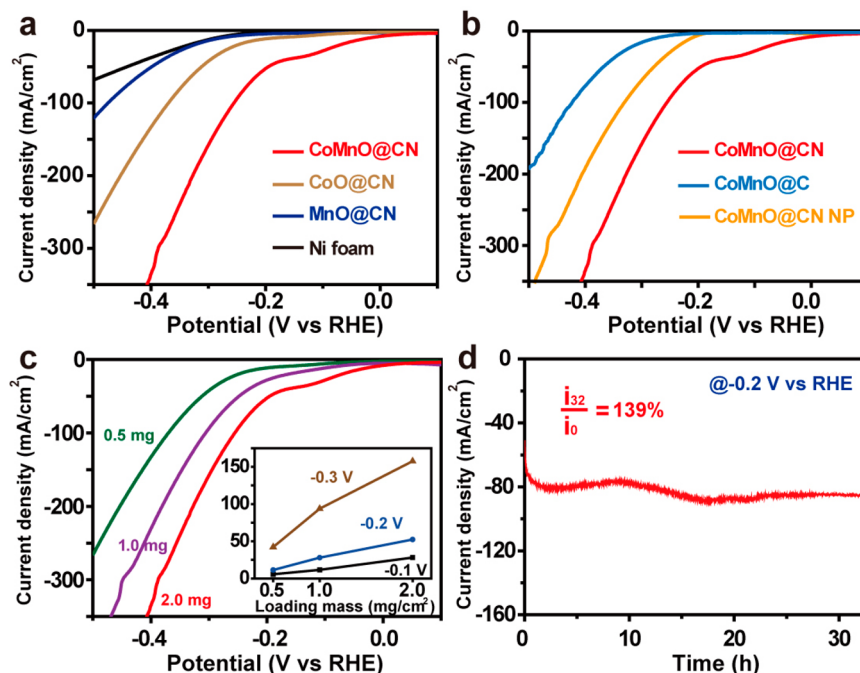
OER Electrocatalytic Performance. The OER activity of the bifunctional CoMnO@CN superlattices were first evaluated by linear sweep voltammetric (LSV) measurement between 1.1 and 1.7 V vs reversible hydrogen electrode (RHE) by a three-electrode system (Methods in the Supporting Information). To fulfill the requirements of efficient ion transport, small pH gradient during electrolysis, and good electrocatalyst stability,[41] an alkaline electrolyte was used for both cathode and anode. Compared to CoO@CN and MnO@CN, the CoMnO@CN superlattices exhibit the best OER performance (Figure 4a, red curve), with an onset potential of 1.46 V vs RHE and a high current density of 308 mA·cm^{-2} at 1.65 V vs RHE. To our best knowledge, this OER current density is the highest among all of the cobalt-based OER catalysts reported previously (Table S1 in the Supporting Information). The effect of the Co/Mn composition ratio on the OER performance was also studied. By changing the Co/Mn ratio from 1:0, 2:1, 1:1, 1:2 to 0:1 in the precursors, the actual Co/Mn ratio in the superlattices was conveniently tuned and determined by ICP (Table S2 in the Supporting Information). The best OER performance was obtained from the Co/Mn ratio of 1:1 (Figure S7a), indicating the optimal composition of the CoMnO@CN superlattices.

The nitrogen-doping effect on the OER performance was further evaluated. In spite of a similar onset potential for both the N-doped CoMnO@CN and undoped CoMnO@C super-lattices, the current density of CoMnO@CN (308 mA·cm^{-2}) is 65% higher than that of the CoMnO@C (186 mA·cm^{-2}) at 1.65 V vs RHE (Figure 4b), attributed to the enhanced

conductivity of the carbon framework by N doping.[42,43] Compared to the disordered CoMnO@CN nanoparticles with similar mass loading (i.e., ∼ 2.0 mg·cm^{-2}) but irregular long-range structures, the OER current density of the CoMnO@CN superlattices is substantially higher (Figure 4b), further confirming that the ordered superlattice structure facilitates the OER catalytic reaction. Moreover, the corresponding Tafel plots demonstrate that the CoMnO@CN superlattices exhibit the lowest Tafel slopes of 97 mV·dec^{-1} among these catalysts (Figure S8a, b), suggesting efficient electron and mass transfer.

Furthermore, the advantage of the CoMnO@CN super-lattices is illustrated by comparison of both the mass loading and the structure effects on the OER performances. At three selected potentials of 1.55, 1.60, and 1.65 V vs RHE, the OER current densities increase almost linearly with different superlattice loading amounts of 0.5, 1.0, and 2.0 mg·cm^{-2} (Figure 4c and inset), confirming that the highly ordered superlattice structure is beneficial for exposure of surface reactive sites, as well as the charge and ion transport toward deep layers of the catalyst. Moreover, the chronoamperometric measurement of the CoMnO@CN superlattices at 1.55 V vs RHE shows a relatively stable trace of OER activity for over 40 h (Figure 4d), although some current density fluctuation is observed during the process, which can be attributed to both the activation and the phase conversion of the catalyst surface during long-time electrochemical tests.[37,44−46] Taken together, these results demonstrate the excellent potentials of using the CoMnO@CN superlattices as an effective and stable OER catalyst.

HER Electrocatalytic Performance. Likewise, the HER activity of the CoMnO@CN superlattices has also been robustly studied. The LSV measurements were carried between

Figure 5. HER electrocatalytic performances. (a) LSV curves for HER of the CoMnO@CN (red curve), CoO@CN (brown curve), and MnO@CN (blue curve) superlattices. The LSV of a blank Ni foam electrode is also plotted as a control (black curve). (b) LSV curves for HER of the CoMnO@CN (red curve), CoMnO@C (blue curve) superlattices, and disordered CoMnO@CN nanoparticles (orange curve). The loading of each catalyst in (a, b) was ~2.0 mg·cm^{-2}. (c) The HER activities of the CoMnO@CN superlattices at different loadings of 0.5, 1.0, and 2.0 mg·cm^{-2}. Inset: specific current densities at −0.1, −0.2, and −0.3 V vs RHE of the CoMnO@CN at different loading masses of 0.5, 1.0, and 2.0 mg·cm^{-2}, respectively. (d) Chronoamperometric measurement of the CoMnO@CN superlattice catalyst at −0.2 V vs RHE.
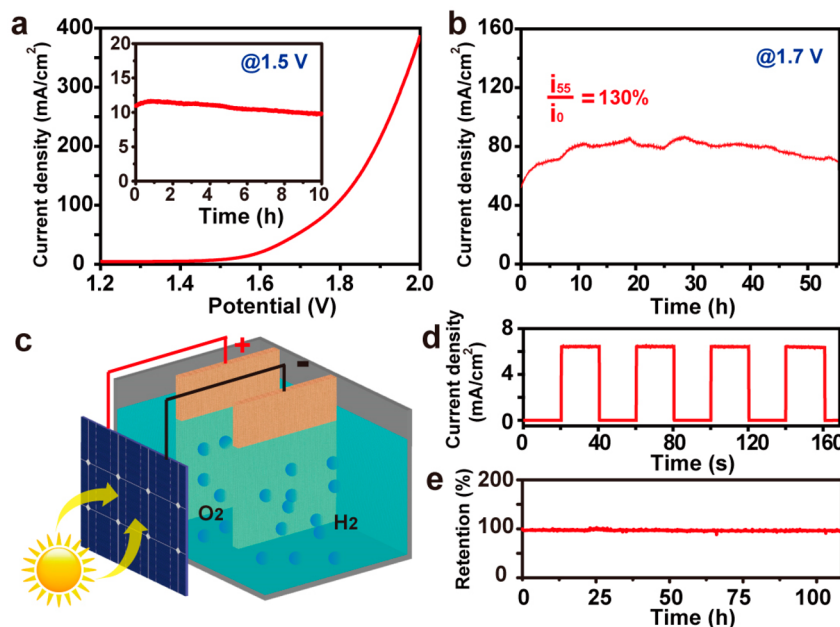
Figure 6. Bifunctional water splitting performances. (a) Overall water splitting characteristics of the CoMnO@CN superlattice catalyst with a two-electrode configuration. Inset: chronoamperometric measurement at 1.5 V applied potential across the electrodes. (b) Chronoamperometric measurement of the overall water splitting at 1.7 V applied potential across the electrodes. (c) Schematic illustration of the solar water splitting cell without additional applied potential, using a commercial planar Si solar cell. (d) Chronoamperometric measurement of the solar water splitting cell under chopped simulated sunlight (AM 1.5G). (e) Current density retention of the solar water splitting cell under continuous sunlight illumination for ~5 days.

−0.5 and 0.1 V vs RHE in 1 M KOH by a three-electrode system. Compared to the CoO@CN and MnO@CN super-lattices, the CoMnO@CN superlattices (Figure 5a, red curve) show the best HER performance, with an overpotential of 71

mV at 20 mA·cm^{-2} and current densities of 28, 52, and 158 mA·cm^{-2} at −100, −200, and −300 mV vs RHE, respectively. This HER performance of the CoMnO@CN superlattices also exceeds most of the earth-abundant material-based HER

catalysts in the literature (Table S3 in the Supporting Information). In addition, the CoMnO@CN superlattices present both much lower overpotentials and much higher current densities than the undoped CoMnO@C superlattices (Figure 5b), in good accord with the expectation that the doping of pyridine-like N atoms in the carbon framework can substantially increase reactive sites for HER.[33] The effect of the Co/Mn composition ratio on the HER performance was also investigated (Figure S7b), from which the CoMnO@CN superlattices also exhibit the best HER performance among all the catalysts with different Co/Mn ratios (Table S4 in the Supporting Information).

The attractive features of the CoMnO@CN superlattices can also be demonstrated in the mass loading and the structural effects on the HER capability. At several selected overpotentials (-0.1, -0.2, and -0.3 V), the current densities of the CoMnO@CN superlattices increase almost linearly with the mass loading ranging from 0.5 to 2 mg·cm^{-2} (Figure 5c and inset), which are also substantially higher than those of the disordered CoMnO@CN nanoparticles with similar mass loading but irregular long-range structures (Figure 5b) confirming that the ordered superlattice structure can also promote the HER catalytic reaction. The CoMnO@CN superlattice catalyst also shows the smallest Tafel slope of 152 mV·dec^{-1} than other samples for HER (Figure S9a, b). Moreover, the chronoamperometric measurement at -0.2 V vs RHE exhibits that the CoMnO@CN superlattices can retain a stable HER activity after 32 h (Figure 5d), suggesting the potential as an attractive HER catalyst.

Bifunctional Catalyst for Electrical and Solar Full Water Splitting. After identifying the OER and HER activities, the bifunctional CoMnO@CN superlattices were investigated as the same electrocatalyst on both electrodes with a two-electrode configuration (Methods in the Supporting Information). At applied biases of 1.7 and 1.8 V, this CoMnO@CN superlattice catalyst shows current densities of 54 and 108 mA·cm^{-2}, respectively (Figure 6a), exceeding most of the previously reported bifunctional electrocatalysts including NiFe LDH,[7] cobalt/cobalt oxide/N-doped carbon hybrids,[11] and NiFeO$_x$/carbon fiber paper[12] (Table S5 in the Supporting Information). At a low applied potential of 1.5 V, a current density of 11 mA·cm^{-2} is obtained, which can be retained over 10 mA·cm^{-2} after 10 h of testing (Figure 6a inset). The long-term stability of the catalyst at large current densities is exhibited by the full water splitting at 1.7 V applied potential. The CoMnO@CN superlattices show excellent stability and slightly increased current density after 55 h of continuous testing (Figure 6b, S10a). The superlattice morphology is largely preserved with good structural ordering without aggregation after the electrochemical stability test (Figure S10b). In comparison, either the CoMnO superlattices without N-doped carbon framework or the disordered CoMnO@CN nanoparticles do not present stable chronoamperometric results, with considerable ($\sim$40–60%) degradation of current densities after 20 h of testing (Figure S11). The bifunctional CoMnO@CN superlattice catalyst performance was also tested in a neutral solution (1 M phosphate buffer saline, pH $\sim$ 7), and the current densities of 28 and 51 mA·cm^{-2} were recorded at applied biases of 1.7 and 1.8 V, respectively (Figure S12).

Finally, the capability of the bifunctional CoMnO superlattice electrocatalyst for solar energy-driven water splitting is exhibited. A commercial planar Si solar cell, with an open-circuit voltage (V_{oc}) of 2.36 V and a photoconversion efficiency of 16.1% (Figure S13a), was used as to convert the solar input (AM 1.5G simulated sunlight) into electrical energy. The solar cell was electrically connected to both electrodes with the CoMnO@CN superlattice bifunctional electrocatalyst for unassisted, full water splitting (Figure 6c, S13b). A current density of 6.43 mA·cm^{-2} was recorded from this solar-driven water-splitting device, which was highly stable and corresponded well with the repeated on–off cycles of simulated AM 1.5G sunlight illumination (Figure 6d). Negligible degradation of the current density was observed after $\sim$5 days of continuous testing (Figure 6e), during which bubbles of oxygen and hydrogen were steadily formed and released from the electrode surface (Movie S1). A solar-to-hydrogen conversion efficiency of $\sim$8.0% was obtained, which can be further increased by using better solar cells with optimized operation conditions.[7,8]

CONCLUSION

In summary, we have synthesized a highly ordered CoMnO@CN superlattice structure as an efficient bifunctional electrocatalyst for water splitting. The uniform CoMnO nanoparticles serve as an excellent OER reagent, with a smaller bandgap, stronger adsorption for OH$^-$, and weaker adsorption for O$_2$ than CoO and MnO. The surrounding nitrogen-doped carbon framework serves as active HER catalytic sites, as well as provides efficient electron and ion transport toward the embedded CoMnO nanoparticles. In the meantime, the ordered superlattice structure with a carbon layer between adjacent CoMnO nanoparticles increases catalytic sites and prevents nanoparticles from aggregation or dissolution. Attributed to these mutual effects of each structural component, this CoMnO@CN superlattice catalyst outperforms most of the earth-abundant material-based OER and HER catalysts and also functions as the best bifunctional catalyst to date, with a high current density and excellent stability. Due to their facile/scalable synthetic method, wide/cheap material availability, and high catalytic activity, these transition metal oxide nanoparticle superlattices suggest attractive promises as substitutes for noble metal-based catalysts toward highly efficient and low-cost electrical or solar-driven water splitting.

ASSOCIATED CONTENT

Ⓢ Supporting Information

The Supporting Information is available free of charge on the ACS Publications website at DOI: 10.1021/jacs.5b07756.

> Methods, additional SEM images, XRD, NEXAFS spectra, DFT calculations, and electrochemical measurements (PDF)
> Movie S1 (AVI)

AUTHOR INFORMATION

Corresponding Author
*gfzheng@fudan.edu.cn

Author Contributions
[⊥] J.L. and Y.W. contributed equally to this work.

Notes
The authors declare no competing financial interest.

■ REFERENCES

(1) Kanan, M. W.; Nocera, D. G. *Science* **2008**, *321*, 1072.

(2) Suntivich, J.; May, K. J.; Gasteiger, H. A.; Goodenough, J. B.; Shao-Horn, Y. *Science* **2011**, *334*, 1383.

(3) Luo, J.; Im, J.-H.; Mayer, M. T.; Schreier, M.; Nazeeruddin, M. K.; Park, N.-G.; Tilley, S. D.; Fan, H. J.; Grätzel, M. *Science* **2014**, *345*, 1593.

(4) Cox, C. R.; Lee, J. Z.; Nocera, D. G.; Buonassisi, T. *Proc. Natl. Acad. Sci. U. S. A.* **2014**, *111*, 14057.

(5) Wang, Y.; Zhou, T.; Jiang, K.; Da, P.; Peng, Z.; Tang, J.; Kong, B.; Cai, W.; Yang, Z.; Zheng, G. *Adv. Energy Mater.* **2014**, *4*, 1400696.

(6) Peng, Z.; Jia, D.; Al-Enizi, A.; Elzatahry, A.; Zheng, G. *Adv. Energy Mater.* **2015**, *5*, 1402031.

(7) Liu, C.; Tang, J.; Chen, H. M.; Liu, B.; Yang, P. *Nano Lett.* **2013**, *13*, 2989.

(8) Wang, Y.; Jing, K.; Zhang, H.; Zhou, T.; Wang, J.; Yang, Z.; Sun, X.; Cai, W.; Zheng, G. *Adv. Science* **2015**, *2*, 1500003.

(9) Jacobsson, T. J.; Fjällström, V.; Sahlberg, M.; Edoff, M.; Edvinsson, T. *Energy Environ. Sci.* **2013**, *6*, 3676.

(10) Lee, Y.; Suntivich, J.; May, K. J.; Perry, E. E.; Shao-Horn, Y. *J. Phys. Chem. Lett.* **2012**, *3*, 399.

(11) Jin, H.; Wang, J.; Su, D.; Wei, Z.; Pang, Z.; Wang, Y. *J. Am. Chem. Soc.* **2015**, *137*, 2688.

(12) Wang, H.; Lee, H.-W.; Deng, Y.; Lu, Z.; Hsu, P.-C.; Liu, Y.; Lin, D.; Cui, Y. *Nat. Commun.* **2015**, *6*, 7261.

(13) Jiang, N.; You, B.; Sheng, M.; Sun, Y. *Angew. Chem., Int. Ed.* **2015**, *54*, 6251.

(14) Yang, Y.; Fei, H.; Ruan, G.; Tour, J. M. *Adv. Mater.* **2015**, *27*, 3175.

(15) Tang, C.; Cheng, N.; Pu, Z.; Xing, W.; Sun, X. *Angew. Chem., Int. Ed.* **2015**, *54*, 9351.

(16) Liang, Y.; Li, Y.; Wang, H.; Zhou, J.; Wang, J.; Regier, T.; Dai, H. *Nat. Mater.* **2011**, *10*, 780.

(17) Gong, M.; Zhou, W.; Tsai, M.-C.; Zhou, J.; Guan, M.; Lin, M.-C.; Zhang, B.; Hu, Y.; Wang, D.-Y.; Yang, J. *Nat. Commun.* **2014**, *5*, 4695.

(18) Liu, Q.; Tian, J.; Cui, W.; Jiang, P.; Cheng, N.; Asiri, A. M.; Sun, X. *Angew. Chem., Int. Ed.* **2014**, *53*, 6710.

(19) Ma, W.; Ma, R.; Wang, C.; Liang, J.; Liu, X.; Zhou, K.; Sasaki, T. *ACS Nano* **2015**, *9*, 1977.

(20) Talapin, D. V.; Lee, J.-S.; Kovalenko, M. V.; Shevchenko, E. V. *Chem. Rev.* **2010**, *110*, 389.

(21) Dong, A.; Chen, J.; Vora, P. M.; Kikkawa, J. M.; Murray, C. B. *Nature* **2010**, *466*, 474.

(22) Jiao, Y.; Han, D.; Ding, Y.; Zhang, X.; Guo, G.; Hu, J.; Yang, D.; Dong, A. *Nat. Commun.* **2015**, *6*, 6420.

(23) Pu, Z.; Liu, Q.; Jiang, P.; Asiri, A. M.; Obaid, A. Y.; Sun, X. *Chem. Mater.* **2014**, *26*, 4326.

(24) Zou, X.; Huang, X.; Goswami, A.; Silva, R.; Sathe, B. R.; Mikmeková, E.; Asefa, T. *Angew. Chem.* **2014**, *126*, 4461.

(25) Zheng, Y.; Jiao, Y.; Zhu, Y.; Li, L. H.; Han, Y.; Chen, Y.; Du, A.; Jaroniec, M.; Qiao, S. Z. *Nat. Commun.* **2014**, *5*, 3783.

(26) Liu, J.; Liu, Y.; Liu, N.; Han, Y.; Zhang, X.; Huang, H.; Lifshitz, Y.; Lee, S.-T.; Zhong, J.; Kang, Z. *Science* **2015**, *347*, 970.

(27) Velev, O. D.; Gupta, S. *Adv. Mater.* **2009**, *21*, 1897.

(28) Wen, T.; Majetich, S. A. *ACS Nano* **2011**, *5*, 8868.

(29) Li, J.; Wang, Y.; Tang, J.; Wang, Y.; Wang, T.; Zhang, L.; Zheng, G. *J. Mater. Chem. A* **2015**, *3*, 2876.

(30) Jiao, Y.; Han, D.; Liu, L.; Ji, L.; Guo, G.; Hu, J.; Yang, D.; Dong, A. *Angew. Chem.* **2015**, *127*, 5819.

(31) Chen, J.; Ye, X.; Oh, S. J.; Kikkawa, J. M.; Kagan, C. R.; Murray, C. B. *ACS Nano* **2013**, *7*, 1478.

(32) Law, M.; Luther, J. M.; Song, Q.; Hughes, B. K.; Perkins, C. L.; Nozik, A. J. *J. Am. Chem. Soc.* **2008**, *130*, 5974.

(33) Ridley, B. A.; Nivi, B.; Jacobson, J. M. *Science* **1999**, *286*, 746.

(34) Wang, J.; Zhou, J.; Hu, Y.; Regier, T. *Energy Environ. Sci.* **2013**, *6*, 926.

(35) Zhang, M.; de Respinis, M.; Frei, H. *Nat. Chem.* **2014**, *6*, 362.

(36) Li, C.-S; Melaet, G.; Ralston, W. T.; An, K.; Brooks, C.; Ye, Y.; Liu, Y.-S.; Zhu, J.; Guo, J.; Alayoglu, S. *Nat. Commun.* **2015**, *6*, 6538.

(37) Song, F.; Hu, X. *J. Am. Chem. Soc.* **2014**, *136*, 16481.

(38) Rödl, C.; Fuchs, F.; Furthmüller, J.; Bechstedt, F. *Phys. Rev. B: Condens. Matter Mater. Phys.* **2009**, *79*, 235114.

(39) Van Elp, J.; Potze, R.; Eskes, H.; Berger, R.; Sawatzky, G. *Phys. Rev. B: Condens. Matter Mater. Phys.* **1991**, *44*, 1530.

(40) Sze, S. M.; Ng, K. K. *Physics of semiconductor devices*; John Wiley & Sons: 2006.

(41) Tian, J.; Liu, Q.; Asiri, A. M.; Sun, X. *J. Am. Chem. Soc.* **2014**, *136*, 7587.

(42) Zhao, Y.; Nakamura, R.; Kamiya, K.; Nakanishi, S.; Hashimoto, K. *Nat. Commun.* **2013**, *4*, 2390.

(43) Gong, K.; Du, F.; Xia, Z.; Durstock, M.; Dai, L. *Science* **2009**, *323*, 760.

(44) Gao, M.; Sheng, W.; Zhuang, Z.; Fang, Q.; Gu, S.; Jiang, J.; Yan, Y. *J. Am. Chem. Soc.* **2014**, *136*, 7077.

(45) Xu, K.; Chen, P.; Li, X.; Tong, Y.; Ding, H.; Wu, X.; Chu, W.; Peng, Z.; Wu, C.; Xie, Y. *J. Am. Chem. Soc.* **2015**, *137*, 4119.

(46) Gao, M.; Sheng, W.; Zhuang, Z.; Fang, Q.; Gu, S.; Jiang, J.; Yan, Y. *J. Am. Chem. Soc.* **2014**, *136*, 7077.